

## Technical Report ARWSB-TR-11037

# High rate deposition of thick CrN and Cr<sub>2</sub>N coatings using modulated pulse power (MPP) magnetron sputtering

Jianliang Lin<sup>1</sup>, William D Sproul<sup>1,2</sup>, John J Moore<sup>1</sup>, Sabrina Lee<sup>3</sup>, Sterling Myers<sup>1</sup>

<sup>1</sup> Advanced Coatings and Surface Engineering Laboratory (ACSEL), Department of Metallurgical and Materials Engineering, Colorado School of Mines, Golden, Colorado

<sup>2</sup> Reactive Sputtering, Inc, 2152 Goya Place, San Marcos, California

<sup>3</sup> U.S. Army Benét Laboratories

December 2010



ARMAMENT RESEARCH, DEVELOPMENT AND ENGINEERING CENTER  
Armaments Engineering & Technology Center  
Weapon Systems & Technology



Approved for public release; distribution is unlimited.

The views, opinions, and/or findings contained in this report are those of the author(s) and should not be construed as an official Department of the Army position, policy, or decision, unless so designated by other documentation.

The citation in this report of the names of commercial firms or commercially available products or services does not constitute official endorsement by or approval of the U.S. Government.

Destroy this report when no longer needed by any method that will prevent disclosure of its contents or reconstruction of the document. Do not return to the originator.

# REPORT DOCUMENTATION PAGE

*Form Approved*  
OMB No. 0704-0188

Public reporting burden for this collection of information is estimated to average 1 hour per response, including the time for reviewing instructions, searching data sources, gathering and maintaining the data needed, and completing and reviewing the collection of information. Send comments regarding this burden estimate or any other aspect of this collection of information, including suggestions for reducing this burden to Washington Headquarters Service, Directorate for Information Operations and Reports, 1215 Jefferson Davis Highway, Suite 1204, Arlington, VA 22202-4302, and to the Office of Management and Budget, Paperwork Reduction Project (0704-0188) Washington, DC 20503.

**PLEASE DO NOT RETURN YOUR FORM TO THE ABOVE ADDRESS.**

1. REPORT DATE (DD-MM-YYYY) 02/05/2011	2. REPORT TYPE Technical	3. DATES COVERED (From - To)
---	-----------------------------	------------------------------

**4. TITLE AND SUBTITLE**

High rate deposition of thick CrN and Cr<sub>2</sub>N coatings using modulated pulse power (MPP) magnetron sputtering

**5a. CONTRACT NUMBER**

**5b. GRANT NUMBER**

**5c. PROGRAM ELEMENT NUMBER**

**6. AUTHOR(S)**

Jianliang Lin (1), William D Sproul (1,2), John J Moore (1), Sabrina Lee (3), Sterling Myers (1)

**5d. PROJECT NUMBER**

**5e. TASK NUMBER**

**5f. WORK UNIT NUMBER**

**7. PERFORMING ORGANIZATION NAME(S) AND ADDRESS(ES)**

U.S. Army ARDEC  
Benet Laboratories, RDAR-WSB  
Watervliet, NY 12189-4000

**8. PERFORMING ORGANIZATION REPORT NUMBER**

ARWSB-TR-11037

**9. SPONSORING/MONITORING AGENCY NAME(S) AND ADDRESS(ES)**

U.S. Army ARDEC  
Benet Laboratories, RDAR-WSB  
Watervliet, NY 12189-4000

**10. SPONSOR/MONITOR'S ACRONYM(S)**

**11. SPONSORING/MONITORING AGENCY REPORT NUMBER**

**12. DISTRIBUTION AVAILABILITY STATEMENT**

Approved for public release; distribution is unlimited.

**13. SUPPLEMENTARY NOTES**

1 ) ACSEL, Department of Metallurgical and Materials Engineering, Colorado School of Mines, Golden, Colorado. 2) Reactive Sputtering, Inc, 2152 Goya Place, San Marcos, California. 3) U.S. Army Benét Laboratories

**14. ABSTRACT**

As a variation of high power pulsed magnetron sputtering technique, modulated pulse power (MPP) magnetron sputtering can achieve a high deposition rate while at the same time achieving a high degree of ionization of the sputtered material with low ion energies. These advantages of the MPP technique can be utilized to obtain dense coatings with a small incorporation of the residual stress and defect density for the thick coating growth. In this study, the MPP technique has been utilized to reactively deposit thick Cr<sub>2</sub>N and CrN coatings (up to 55  $\mu$ m) on AISI 440C steel and cemented carbide substrates in a closed field unbalanced magnetron sputtering system.

**15. SUBJECT TERMS**

Modulated pulse power (MPP), high power pulsed magnetron sputtering (HPPMS), high-power impulse magnetron sputtering (HIPIMS), thick coating, CrN coating, Cr<sub>2</sub>N coating, scratch, wear

**16. SECURITY CLASSIFICATION OF:**

a. REPORT  
U/U

b. ABSTRACT  
U

c. THIS PAGE  
U

**17. LIMITATION OF ABSTRACT**

U

**18. NUMBER OF PAGES**

39

**19a. NAME OF RESPONSIBLE PERSON**

Jianliang Lin

**19b. TELEPHONE NUMBER (Include area code)**

303-273-3178

INSTRUCTIONS FOR COMPLETING SF 298

**1. REPORT DATE.** Full publication date, including day, month, if available. Must cite at least the year and be Year 2000 compliant, e.g., 30-06-1998; xx-08-1998; xx-xx-1998.

**2. REPORT TYPE.** State the type of report, such as final, technical, interim, memorandum, master's thesis, progress, quarterly, research, special, group study, etc.

**3. DATES COVERED.** Indicate the time during which the work was performed and the report was written, e.g., Jun 1997 - Jun 1998; 1-10 Jun 1996; May - Nov 1998; Nov 1998.

**4. TITLE.** Enter title and subtitle with volume number and part number, if applicable. On classified documents, enter the title classification in parentheses.

**5a. CONTRACT NUMBER.** Enter all contract numbers as they appear in the report, e.g. F33615-86-C-5169.

**5b. GRANT NUMBER.** Enter all grant numbers as they appear in the report, e.g. 1F665702D1257.

**5c. PROGRAM ELEMENT NUMBER.** Enter all program element numbers as they appear in the report, e.g. AFOSR-82-1234.

**5d. PROJECT NUMBER.** Enter all project numbers as they appear in the report, e.g. 1F665702D1257; ILIR.

**5e. TASK NUMBER.** Enter all task numbers as they appear in the report, e.g. 05; RF0330201; T4112.

**5f. WORK UNIT NUMBER.** Enter all work unit numbers as they appear in the report, e.g. 001; AFAPL30480105.

**6. AUTHOR(S).** Enter name(s) of person(s) responsible for writing the report, performing the research, or credited with the content of the report. The form of entry is the last name, first name, middle initial, and additional qualifiers separated by commas, e.g. Smith, Richard, Jr.

**7. PERFORMING ORGANIZATION NAME(S) AND ADDRESS(ES).** Self-explanatory.

**8. PERFORMING ORGANIZATION REPORT NUMBER.** Enter all unique alphanumeric report numbers assigned by the performing organization, e.g. BRL-1234; AFWL-TR-85-4017-Vol-21-PT-2.

**9. SPONSORING/MONITORS AGENCY NAME(S) AND ADDRESS(ES).** Enter the name and address of the organization(s) financially responsible for and monitoring the work.

**10. SPONSOR/MONITOR'S ACRONYM(S).** Enter, if available, e.g. BRL, ARDEC, NADC.

**11. SPONSOR/MONITOR'S REPORT NUMBER(S).** Enter report number as assigned by the sponsoring/ monitoring agency, if available, e.g. BRL-TR-829; -215.

**12. DISTRIBUTION/AVAILABILITY STATEMENT.** Use agency-mandated availability statements to indicate the public availability or distribution limitations of the report. If additional limitations/restrictions or special markings are indicated, follow agency authorization procedures, e.g. RD/FRD, PROPIN, ITAR, etc. Include copyright information.

**13. SUPPLEMENTARY NOTES.** Enter information not included elsewhere such as: prepared in cooperation with; translation of; report supersedes; old edition number, etc.

**14. ABSTRACT.** A brief (approximately 200 words) factual summary of the most significant information.

**15. SUBJECT TERMS.** Key words or phrases identifying major concepts in the report.

**16. SECURITY CLASSIFICATION.** Enter security classification in accordance with security classification regulations, e.g. U, C, S, etc. If this form contains classified information, stamp classification level on the top and bottom of this page.

**17. LIMITATION OF ABSTRACT.** This block must be completed to assign a distribution limitation to the abstract. Enter UU (Unclassified Unlimited) or SAR (Same as Report). An entry in this block is necessary if the abstract is to be limited.

## **TABLE OF CONTENTS**

Abstract.....	1
Introduction .....	3
Experimental Details .....	6
Results and Discussion .....	10
Composition and microstructure.....	10
Mechanical and Tribological Properties .....	16
Conclusions .....	21
References .....	22

## **LIST OF TABLES**

Table 1: The deposition conditions for the Cr interlayer, CrN and Cr <sub>2</sub> N coatings .....	25
--	----

## LIST OF FIGURES

Figure 1: The target voltage, current and power waveforms during one modulated pulse used for the depositions .....	26
Figure 2a: XRD patterns of the MPP sputtered CrN coatings with different coating thicknesses .....	26
Figure 2b: XRD patterns of the MPP sputtered Cr <sub>2</sub> N coatings with different coating thicknesses .....	27
Figure 3: Effect of the coating thickness on the average grain size of the MPP CrN and Cr <sub>2</sub> N coatings.....	28
Figure 4: Dependence of the residual stresses of the MPP CrN and Cr <sub>2</sub> N coatings on the coating thickness. ....	28
Figure 5: Cross-sectional SEM micrographs of the MPP sputtered CrN coatings with different thicknesses a) 10 µm, b) 20 µm, c) 30 µm and d) 55 µm.....	29
Figure 6: Cross-sectional SEM micrographs of the MPP sputtered Cr <sub>2</sub> N coatings with different thicknesses a) 10 µm, b) 20 µm, c) 30 µm and d) 55 µm.....	31
Figure 7: Cross-sectional SEM micrographs of the microstructure of the 55 µm a) CrN and b) Cr <sub>2</sub> N coatings as observed in the box marked in Figure 5d and Figure 6d .....	32
Figure 8: Top view SEM micrographs of the 55 µm a) CrN and b) Cr <sub>2</sub> N coatings .....	33
Figure 9: Effect of the coating thickness on the average surface roughness of the MPP sputtered CrN and Cr <sub>2</sub> N coatings.....	34
Figure 10: a) Hardness and Young's modulus, and b) the H/E ratios of the MPP sputtered CrN and Cr <sub>2</sub> N coatings with different coating thicknesses .....	35
Figure 11: Cross-sectional SEM micrographs showing the nanoindentation test performed on the polished cross-section of the 20 µm CrN coating along the coating thickness .....	36
Figure 12: Fricition force versus the applied load during the progressive load scratch tests performed on the CrN coatings deposited on AISI 440C steel substrate with different coating thicknesses .....	36
Figure 13: Fricition force versus applied load during the progressive load scratch tests performed on the 55 µm CrN and Cr <sub>2</sub> N coatings deposited on WC-Co substrate. (The insert SEM micrographs show the beginning of the adhesive failure of the Cr <sub>2</sub> N coating and the end of the scratch track of the CrN coating) .....	37
Figure 14: Coefficient of friction and wear rate of the MPP sputtered a) CrN and b) Cr <sub>2</sub> N coatings with different coating thicknesses.....	37

## **Abstract:**

As a variation of high power pulsed magnetron sputtering technique, modulated pulse power (MPP) magnetron sputtering can achieve a high deposition rate while at the same time achieving a high degree of ionization of the sputtered material with low ion energies. These advantages of the MPP technique can be utilized to obtain dense coatings with a small incorporation of the residual stress and defect density for the thick coating growth. In this study, the MPP technique has been utilized to reactively deposit thick Cr<sub>2</sub>N and CrN coatings (up to 55 μm) on AISI 440C steel and cemented carbide substrates in a closed field unbalanced magnetron sputtering system. High deposition rates of 15 and 10 μm per hour have been measured for the Cr<sub>2</sub>N and CrN coating depositions, respectively, using a 3 kW average target power (16.7 W/cm<sup>2</sup> average target power density), a 50 mm substrate to target distance and an Ar/N<sub>2</sub> gas flow ratio of 3:1 and 1:1. The CrN coatings showed a denser microstructure than the Cr<sub>2</sub>N coatings, whereas the Cr<sub>2</sub>N coatings exhibited a smaller grain size and surface roughness than those of the CrN coatings for the same coating thickness. The compressive residual stresses in the CrN and Cr<sub>2</sub>N coatings increased as the coating thickness increased to 30 μm and 20μm, respectively, but for thicker coatings, the stress gradually decreased as the coating thickness increased. The CrN coatings exhibited an increase in the scratch test critical load as the thickness was increased. Both CrN and Cr<sub>2</sub>N coatings showed a decrease in the hardness and an increase in the sliding coefficient of friction as the coating thickness increased from 2.5 to 55 μm. However, the wear rate of the CrN coatings decreased significantly as the coating thickness was increase to 10 μm or higher. The 10-55 μm CrN coating exhibited low wear rates in the range of  $3.5\text{--}5 \times 10^{-7}$

$\text{mm}^3\text{N}^{-1}\text{m}^{-1}$ . To the contrary, the Cr<sub>2</sub>N coating exhibited relatively poor wear resistance in that high wear rates in the range of  $3.5$  to  $7.5 \times 10^{-6} \text{ mm}^3\text{N}^{-1}\text{m}^{-1}$  were observed for different thicknesses.

## **1. Introduction**

It is highly desirable to deposit hard protective coatings at a high deposition rate to increase the cost effectiveness of the process and to increase the life and performance of the coating by applying a relatively thick coating (e.g.  $> 6 \mu\text{m}$ ). There are several widely used thick coating preparation methods, for example electroplating [1], thermal plasma spraying [2], Sol-Gel technique [3], cathodic arc deposition (CAD) [4,5], and chemical vapor deposition (CVD) [6,7], etc. These techniques have good process stability and in many cases low costs, and they have been adapted for industrial production. Nevertheless, some of the above techniques such as electroplating are not environmental friendly, and the coatings can exhibit low density, poor adhesion, and poor properties. Magnetron sputtering, a physical vapor deposition (PVD) vacuum coating technique, in the right application and practiced by one skilled in the art, can overcome many of the above listed disadvantages for the different coating techniques.

Sputtering is a very flexible and effective deposition process for depositing various metallic and compound thin films for industrial surface engineering applications. There are many advantages to the sputter deposition technique such as the ability to deposit coatings at low substrate temperatures or to control the structure and properties of the deposited coatings by controlling the deposition parameters. However compared to other PVD processes such as CAD, the sputter deposition rate usually is not as high as it is for CAD. In addition, the thickness of sputter deposited coatings is often limited by the intrinsic stress that builds up in the coating during the deposition combined with thermal stresses generated by differences in the coefficient of thermal expansion (CTE) between the coating and the substrate material [8,9]. Typically for hard coatings such as

titanium nitride (TiN), the combined stress in the films generally limits the coating thickness to about 6-7  $\mu\text{m}$  [10].

In recent years, high-power pulsed magnetron sputtering (HPPMS) (also known as high-power impulse magnetron sputtering (HIPIMS)) [11,12,13,14] and modulated pulse power magnetron sputtering (MPP) techniques [15,16,17,18,19,20], a variation of HPPMS, have shown great advantages as compared to the conventional dc magnetron sputtering (dcMS) and pulsed dc magnetron sputtering (PMS) techniques [18]. Specifically the HPPMS/HIPIMS and MPP techniques can produce a high degree of ionization of the sputtered species, and this high ion flux can be used to improve the structure and properties of the sputtered coating.

The difference between the originally introduced version of HPPMS by Kouznetsov and co-workers [21] and the MPP technique is basically in the magnitude, duration, and shape of the high power pulses. With the Kouznetsov technique, a single short high power pulse, on the order of 100  $\mu\text{s}$  in duration is applied to the sputtering cathode, and the magnitude of the pulse is on the order of 1.0 to 3.0  $\text{kW cm}^{-2}$  in order to achieve a high degree of ionization of the sputtered material. With the MPP technique the pulse is typically a multistep pulse where a weakly ionized plasma is first ignited and then the plasma transitions to a highly ionized plasma by increasing the voltage applied to the cathode. The duration of the MPP pulse can be as long as 3,000  $\mu\text{s}$ , and the peak power is typically in the 100 to 800 kW range. Because HPPMS and MPP deposition techniques are pulse processes, the pulse repetition rate is adjusted so that the average power applied to the target is similar to what it is for conventional magnetron sputtering processes in order not to overheat the sputtering target.

These large number of metallic ions not only can densify the coating by the enhanced ion bombardment, but also can be utilized to pre-clean the substrate at the beginning of the film growth and thereby enhancing the bonding strength between the coating and the substrate [22]. The large number of metallic ions arriving at the substrate also means that lower substrate bias voltages can be used during deposition, which reduces the stress and damage in the deposited coating and allows thicker films to be deposited [23].

Early HPPMS work showed that the deposition rate for the HPPMS films compared to similar films deposited by convention magnetron sputtering at the same average power was much lower [12,24]. However, it has been demonstrated that for some MPP depositions that it is possible to deposit coatings at rates close to or greater than the rate for conventional magnetron sputtering for the same average power. [15,16,17,20]. Enhanced MPP deposition rates for sputtered Cu, graphite, Ti, and Cr materials as compared to dcMS have been reported [15,16,17,20].

Even though the MPP peak power is not as high as it is in the Kouznetsov approach, the MPP technique can still produce a high degree of ionization of the sputtered species [18,19,20]. Additionally, unlike the traditional HPPMS/HiPIMS plasma, which contains a wide range of ion energy distributions (up to 100 eV) [25], plasma diagnostics of MPP plasmas for sputtering a Cr target in either an Ar or Ar/N<sub>2</sub> mixture showed that the majority of the ions in a MPP plasma are the target metallic ions, which exhibit a low peak ion energy in a range of 2-5 eV without the presence of the high energy ions [18,19,20]. Thus it is expected that it is practical to deposit thick coatings using the MPP technique by taking advantage of its high deposition rate and

ideal low energy/high ion flux bombardment to achieve coatings with a dense microstructure and low stress and defect incorporation.

In this study, we have explored the possibility of reactive sputtering thick nitride coatings using the MPP technique. In this regard, thick CrN and Cr<sub>2</sub>N coatings (up to 55 μm thick) were deposited in a closed field unbalanced magnetron sputtering system (CFUBMS) using the MPP magnetron sputtering technique. High deposition rates of 15 and 10 μm per hour have been obtained for the Cr<sub>2</sub>N and CrN depositions, respectively, using a 3 kW average target power, a 50 mm substrate to target distance and an Ar/N<sub>2</sub> gas ratio of 3:1 and 1:1. The coatings were characterized by means of electron probe micro-analysis (EPMA), x-ray diffraction (XRD), field-emission scanning electron microscopy (FESEM), nanoindentation, scratch test, and ball-on-disk wear test in an effort to correlate the microstructure, residual stress, mechanical and tribological properties with the coating thickness.

## 2. Experimental details

The deposition system is a CFUBMS system equipped with two rectangular unbalanced magnetrons (320 mm× 127 mm) which are installed opposite one another with a distance of 240 mm between them. A metal Cr target (99.99% purity) was powered by a MPP generator (SOLO/AXIS-180<sup>TM</sup> Pulsed DC Plasma Generator, Zpulser LLC), while the other magnetron was not powered but kept in the system to create a closed magnetic field to reduce losses of electrons to the chamber wall and thereby enhancing the plasma density.

AISI 440C steel (HRC=22) and WC-Co (HRC=55) coupons were used as the

substrates. The hardness of the bulk substrates was measured using a Vicker indenter. After mechanical polishing to a mirror finish (with a surface roughness of about 8-10 nm), the substrates were ultrasonically cleaned in acetone and ethylene for 15 min, respectively. The substrates were mounted on a substrate holder and installed at a distance of 50 mm from the target surface. An Ar plasma etching process was used to further clean the substrate surface for improving the coating adhesion. The etching process was carried out at a pressure of 1.33 Pa with a conventional pulsed dc bias of -650 V (200 kHz and 1.0  $\mu$ s reverse time) applied for 40 mins, which generated 370 W of power and 0.8 A of current on the substrate holder.

During the deposition, the working pressure was maintained at 0.67 Pa. The negative dc substrate bias voltage was maintained constantly at -50 V. In general, a significant large ion current (can be up to 50 A) passes through the substrate in the HPPMS/MPP deposition due to the highly ionized plasma, as compared to 1-2 A in the conventional dc magnetron sputtering [26,27]. To avoid the voltage drop during the deposition, a dc bias power supply (AXIS, Zpulser LLC.), which can handle a maximum current of 50 A with the arc suppression capability, was used for all the depositions.

The pulse length of the MPP pulse used in the study was 1000  $\mu$ s, which contains a 500  $\mu$ s weakly ionized stage and a 500  $\mu$ s strongly ionized stage as shown in Fig. 1. Before the depositions of the CrN and Cr<sub>2</sub>N coatings, a Cr interlayer with a thickness of about 400-500 nm was deposited for improving the adhesion between the coating and substrate. For the Cr layer deposition, the Cr target was powered at an average target power of 1.5 kW. However, a high peak target current and power of 200 A and 150 kW,

respectively, were applied on the target during the high ionization period in an effort to achieve a high degree of ionization and a high plasma density (as summarized in Table 1). The repetition rate of the pulse was 30 Hz. A TekVISA digital oscilloscope (TDS3014) was used to measure the peak and mean substrate ion current densities ( $I_{sub}$ ) during the coating depositions. High peak and mean  $I_{sub}$  of 350 and 66 mA/cm<sup>2</sup>, respectively, were measured during the Cr layer deposition.

After the Cr layer deposition, CrN and Cr<sub>2</sub>N coatings with various thicknesses (2.5 to 55  $\mu$ m) were reactively deposited by sputtering of the Cr target using MPP with an average target power of 3 kW (16.7 W/cm<sup>2</sup> average target power density) in an Ar/N<sub>2</sub> mixture at an Ar to N<sub>2</sub> flow ratio of 1:1 and 3:1, respectively. The length and shape of the MPP pulses used for the CrN and Cr<sub>2</sub>N coating depositions are the same as the one used for the Cr adhesion layer deposition (Fig. 1). However, relatively lower peak power and peak current were utilized to guarantee the reactive sputtering process stability. The detailed deposition and pulsing parameters for the Cr adhesion layer, CrN and Cr<sub>2</sub>N coating depositions are summarized in Table 1.

The chemical composition of the coatings was measured by EPMA at a 15 kV voltage and a 10  $\mu$ m beam size, with the calibration of Cr and TiN standards. The crystal structure of the coatings was determined by XRD using a SIEMENS X-ray diffractometer (Model KRISTALLOFLEX-810) operated with K-alpha Cu radiation (30 kV and 20 mA) in the conventional Bragg-Bentano mode. The residual stress of the coatings was measured by glancing incident angle XRD (GIXRD) in the same X-ray diffractometer using the  $\sin^2 \psi$  method [28]. The (200) peak of the CrN coatings (with a standard peak at 43.7 degree) and the (111) peak of the Cr<sub>2</sub>N coatings (with a standard

peak at 42.6 degree) were selected to derive the variation of the lattice parameter in terms of different incident angles (1 to 10 degrees) for the stress measurement. The grain sizes of the CrN and Cr<sub>2</sub>N coatings were estimated from the (200) and (111) diffraction peaks, respectively, using the Scherrer equation [29]. The thickness, surface morphology and cross-sectional microstructure of the CrN and Cr<sub>2</sub>N coatings were characterized using a JSM-7000F FESEM operated at a 5 kV accelerating voltage. The mean surface roughness ( $R_a$ ) was evaluated by a Veeco 3D surface profilometer by sampling from a 500  $\mu\text{m}^2$  region from the coating surface. For each sample, five measurements were made to obtain the mean value and the standard deviation.

Hardness (H) and Young's modulus (E) values of the coatings deposited on the AISI 440C tool steel were characterized by nanoindentation using a MTS nano-indenter XPII equipped with a Berkovich diamond indenter. The tester was calibrated by using glass and fused silica samples. The indentations were carried out on the surface of the coating with an indentation depth less than 10% of the coating thickness to minimize the influence of the substrate. However, for the thicker coatings ( $\geq 10 \mu\text{m}$ ), the nanoindentation tests were also carried out on the polished cross-section of the coatings, which was mounted in the thermosetting resins and polished down to a mirror finish. The depth of these indentation tests was 300 nm. More than 20 indentations were precisely performed on the cross-section of the coatings.

The adhesion strength of the coatings deposited on AISI 440C tool steel and WC-Co was evaluated by a Teer scratch tester using a Rockwell C indent tip (tip radius R=200  $\mu\text{m}$ , and conical angle=120°). The applied load was increased from 5 N up to 100 N at a rate of 100 N/min and the scratch length was 6 mm. The critical load was

evaluated by monitoring the acoustic emission (AE) signal change during the progressive-loading process. The obtained scratch tracks were examined by FESEM to identify the coating failure morphologies.

Ball-on-disk wear resistance tests were performed on the coatings deposited on the AISI 440C steel using a microtribometer (Center for Tribology, Inc) in an ambient air atmosphere without a lubricant (a relative humidity of  $25\pm1$  % and a temperature of  $25\pm1$  °C). The sliding counterpart was a 5 mm  $\text{Al}_2\text{O}_3$  ball. The normal load applied on the coating surface was  $10\pm0.5$  N which was controlled by a load suspension system. A high rotation speed of 200 rpm of the specimen was used, and the travel lengths for the CrN and  $\text{Cr}_2\text{N}$  coatings were 2000 m and 800 m, respectively. The average coefficient of friction (COF) values were read from the steady sliding state in the tests. After the wear tests, the wear tracks were examined using a Veeco 3D surface profilometer to measure the wear volume ( $\text{mm}^3$ ) and calculate the wear rate ( $\text{mm}^3\text{N}^{-1}\text{m}^{-1}$ ).

### **3. Results and discussion**

#### **3.1 Composition and microstructure**

The chemical composition of the CrN and  $\text{Cr}_2\text{N}$  coatings was measured by EPMA. The O and Ar contents in the coatings are below 1 at.%. It was found that the N/Cr ratios of the CrN and  $\text{Cr}_2\text{N}$  coatings showed small variations in a range of 1.1 to 1.05 and 0.5 to 0.55, respectively. The results revealed that near stoichiometric CrN and  $\text{Cr}_2\text{N}$  coatings were obtained. The chemical composition of the coatings is almost independent of the variation of the thickness of the coating or the deposition time in the MPP sputtering.

Fig. 2 shows the XRD patterns of the MPP sputtered CrN and Cr<sub>2</sub>N coatings with different thicknesses. As shown in Fig. 2a, all CrN coatings exhibited a NaCl type face center cubic (fcc) structure (JCPDS 11-0065 [30]). The 5 and 10 μm CrN coatings exhibited a strong (311) reflection. As reported in various reports that the fcc CrN coating would grow toward the (111) orientation to lower the strain energy in the energetic ion assisted deposition [31]. However, according to Nouveauc et al. [32], the development of the (311) orientation parallel to the sample surface in the CrN coatings can be due to the difference of growth rates between the two crystallographic planes and by a preferential re-sputtering of the N atoms lying on the (111) planes. As the thickness of the coating was increased to 20 and 30 μm, the coatings exhibited a polycrystalline structure with strong (111) and (200) reflections due to the competition growth between different crystallographic planes to minimize both strain and surface energies as the thickness increased. Further increasing the coating thickness from 30 to 55 μm, the preferred orientation of the coatings gradually changed to a (200) orientation at the expense of (311) and (111) planes (Fig. 3a). Since the (200) plane is the densest plane with the lowest surface energy in the fcc CrN structure [33], the final development of a (200) orientation for the very thick CrN coatings can be attributed to the lattice strain relaxation after a longer deposition time and therefore the minimization of the surface energy becomes dominate.

As shown in Fig. 2b, all Cr<sub>2</sub>N coatings exhibited a hexagonal structure with a strong (111) orientation centered at 42.3 degree (JCPDS 35-0803 [34]). The coatings with the thicknesses less than 20 μm also showed small (112) and (302) reflections.

No obvious peak shifting was identified for both CrN and Cr<sub>2</sub>N coatings as the

thickness of the coating increased, indicating a consistent chemical composition in the coatings as the thickness was increased. It can be seen that the Cr<sub>2</sub>N coatings exhibited more broadened diffraction peaks than the CrN coatings, which can be related to a smaller grain size or different residual stress levels in the Cr<sub>2</sub>N coatings (Fig. 2).

The average grain size of the coatings was plotted as a function of the thickness of the coating, as shown in Fig. 3. The average grain size of the CrN coating increased rapidly from 5 nm to 30 nm as the coating thickness increased from 15 μm to 20 μm, and gradually increased to 42 nm at a thickness of 55 μm. In contrast, the Cr<sub>2</sub>N coatings exhibited smaller average grain size than the CrN coatings, which slightly increased from 12 to 20 nm as the coating thickness increased from 5 μm to 55 μm.

Fig. 4 shows the residual stress of the CrN and Cr<sub>2</sub>N coatings deposited on AISI 400C steel with different thicknesses. All coatings exhibited a compressive residual stress. The residual stress of the CrN coatings increased rapidly from -2.2 GPa to -5.0 GPa as the coating thickness increased from 2.5 μm to 20 μm and slowly reached the maximum value of -5.5 GPa at a thickness of 30 μm. As the coating thickness was further increased beyond 30 μm, the residual stress gradually decreased to around -4 GPa at a thickness of 55 μm. The residual stress of the Cr<sub>2</sub>N coatings exhibited similar revolution trend to that of the CrN coatings. The residual stress in the Cr<sub>2</sub>N coatings increased from -2.7 GPa to -4.5 GPa as the coating thickness increased to 20 μm and then gradually decreased to -2.1 GPa at a thickness of 55 μm. Nevertheless, most Cr<sub>2</sub>N coatings exhibited relatively smaller residual stresses than the CrN coatings for the same coating thickness, except for the 2.5 μm thin film.

The residual stress in the magnetron sputtered coatings generally originates from

the thermal stress and intrinsic stress [8]. The internal stress is generated from the accumulation of the defects, in the form of vacancies, interstitial atoms, and point and line dislocations by the kinetic neutral and ion bombardment [8,35]. The thermal stress is mainly generated by the mismatch between the substrate and the coating during the cooling period after the deposition due to the difference in the CTE values between the substrate and coating material [36]. It has been reported that the CTE for the 440 C stainless steel substrate is  $10.2 \times 10^{-6} \text{ } ^\circ\text{C}^{-1}$  [37], while the CTE values for the CrN and Cr<sub>2</sub>N coatings are  $2.3 \times 10^{-6} \text{ } ^\circ\text{C}^{-1}$  and  $9.5 \times 10^{-6} \text{ } ^\circ\text{C}^{-1}$ , respectively [38,39,40]. Since the deposition and pulsing parameters are the same for the CrN and Cr<sub>2</sub>N coating depositions, the compressive stress caused by ion peening can be assumed similar. Therefore, it is expected that higher thermal residual stress was generated in the CrN coatings upon cooling from the deposition temperature due to the much larger CTE difference between 440C steel substrate and CrN coatings, and which possibly accounts for their higher final residual stresses, as shown in Fig. 4. This result is consistent with the early study conducted by Herr et al., [41] who have shown that the Cr<sub>x</sub>N<sub>y</sub> coatings deposited on steel substrate exhibited increased residual stress with an increase in the N content due to the increased CTE difference between the coating and the substrate.

In another aspect, as the coating grows thicker, the longer deposition time and gradually increased substrate temperature allow the buried defects (e.g. the Schottky defects and Frenkel disorder) to have more time to diffuse through the crystal structure and arrive at dislocation cores or grain boundaries where they become absorbed [42]. The absorption or annihilation of the defects releases the stress [43]. Therefore, the competition of the accumulation and annihilation of the residual stress contributes to the

evolution of the residual stress in the coatings as the coating grows thicker.

As can be seen in Fig. 4, the residual stresses of the CrN and Cr<sub>2</sub>N coatings increased as the coating thickness was increased to 20 μm due to the fast accumulation of the residual stress. As the deposition time was increased (the coating grew thicker), the contribution of the absorption or annihilation of the defects to release the stress becomes important. This contribution results in a decrease in the rate of the increase of the residual stress as the CrN coating thickness was increased from 20 μm to 30 μm. As the CrN and Cr<sub>2</sub>N coatings grew thicker (above 30 μm and 20 μm respectively), the rate of the annihilation of the stress possibly overwhelms the rate of the accumulation of the stress, which lead to a decrease in the coating residual stress.

Fig. 5 and Fig. 6 show the cross-sectional SEM micrographs of CrN and Cr<sub>2</sub>N coatings deposited on AISI 440C tool steel with different thicknesses of 10, 20, 30 and 55 μm respectively. The coatings with thicknesses less than 10 μm exhibited a similar microstructure. Overall, all CrN and Cr<sub>2</sub>N coatings exhibited dense microstructures. However, a more pronounced short and disordered columnar grain growth is evident in the CrN coatings (Fig. 5), whereas the Cr<sub>2</sub>N coatings exhibited a fine grain structure with less features (Fig. 6). This observation is similar to former reported results on the dc and pulsed dc magnetron sputtered Cr<sub>2</sub>N and CrN coatings [44,45], as well as the Cr<sub>2</sub>N coating deposited by the HIPIMS technique with a peak power density higher than 137 Wcm<sup>-2</sup> [46]. It is also noted that there is no significant increase in the grain size as the thicknesses of the CrN and Cr<sub>2</sub>N coatings were increased, which is consistent with the observation in the XRD patterns.

A small area of the 55 μm CrN and Cr<sub>2</sub>N coatings (as indicated by the box in Figs.

5d and 6d) were examined at a higher magnification, as shown in Figs. 7a and 7b respectively. It can be seen that the 55  $\mu\text{m}$  CrN coating exhibited a typical columnar grain structure. In addition, a large number of granular shaped nano grains (<10 nm) can be seen within the large columnar grains (Fig. 7a). The reason for the formation of these nanograins is not clear. However, one possibility is that the high ion flux bombardment from the MPP plasma increases the adatoms mobility and thereby creates a large number of renucleation sites during the film growth. It should be note that the grain size estimated from the XRD patterns using the Scherrer equation is smaller than the width of the columnar grains as observed in the SEM image. Therefore, it is assumed that these nano featured grains (Fig. 7a) and the compressive internal stress in the CrN coatings also contribute to the diffraction peak broadening (Fig. 2).

On the other hand, the 55  $\mu\text{m}$  Cr<sub>2</sub>N coating exhibited a less featured columnar structure as shown in Fig. 7b. The grain size of the Cr<sub>2</sub>N coating is finer than that of the CrN coatings, which is consistent with the results estimated from the XRD patterns (Fig. 3). The SEM characterization also indicated that the 55  $\mu\text{m}$  Cr<sub>2</sub>N coating exhibited a less dense microstructure than the CrN coating, where some porosity was observed (Fig. 7b).

Fig. 8 shows the SEM micrographs of the surface morphologies of the 55  $\mu\text{m}$  CrN and Cr<sub>2</sub>N coatings. The surface of the 55  $\mu\text{m}$  CrN coating exhibited a striated feature of the grain grown in random directions (Fig. 8a). This kind of surface feature is similar to the Cr coatings deposited using the MPP process [20] and Nb coatings deposited using the ultra-high vacuum cathodic arc process [47]. As shown in Fig. 8b, the 55  $\mu\text{m}$  Cr<sub>2</sub>N coating exhibited a completely different surface morphology, in which the hexagon

featured network of the grains is evident from the image, confirming the formation of the hexagonal  $\beta$ -Cr<sub>2</sub>N phase in the coating (Fig. 2b).

The  $R_a$  values of the CrN and Cr<sub>2</sub>N coatings measured for a 500  $\mu\text{m}^2$  surface area are plotted in Fig. 9 as a function of the coating thickness. As the coating thickness increased, the  $R_a$  values of both coatings increased. The increase in the surface roughness as the CrN and Cr<sub>2</sub>N coatings grew thicker is mainly due to the grain growth (Fig. 3) and the increased number of macro particles on the surface (as observed under the optical profilometer) as the coatings grew thicker. Nevertheless, the Cr<sub>2</sub>N coatings exhibited lower  $R_a$  values than the CrN coatings at the same coating thickness.

### 3.2 Mechanical and tribological properties

Fig. 10a shows the hardness and Young's modulus of the MPP sputtered CrN and Cr<sub>2</sub>N coatings as a function of the coating thickness. For the same coating thickness, the CrN coatings exhibited lower hardness and Young's modulus values than those of the Cr<sub>2</sub>N coatings. The 2.5  $\mu\text{m}$  CrN and Cr<sub>2</sub>N coatings exhibited a high hardness of 26.2 GPa and 27.3 GPa, respectively. A gradual decrease in the coating hardness and Young's modulus with an increase in the coating thickness was observed for both CrN and Cr<sub>2</sub>N coatings. The 55  $\mu\text{m}$  CrN and Cr<sub>2</sub>N coatings exhibited a hardness of 22.2 and 24.5 GPa, respectively.

The reduction of the coating hardness can be attributed to several factors. As the coating thickness was increased, the increase in the average grain size of the coating will probably contribute to a decrease in the coating hardness according to the Hall-Petch effect [48]. In another aspect, the decrease in the coating hardness as the

coating grew thicker, may also result from the release of the compressive stress in the coatings by the absorption or annihilation of the defects with the increased coating temperature and deposition time. Another possibility is that nucleated dislocations have to glide forward in order for the indenter to move forward during indentation tests. For the thin films, dislocations quickly hit the film-substrate interfaces and are blocked there. Once blocked, these dislocations will make further dislocation nucleation and glide more difficult, which will increase the measured coating hardness.

It has been shown that the ability of a coating to resist mechanical degradation and failure is improved by a high H/E ratio (resistance against elastic strain to failure) [49,50], which implies a longer ‘elastic strain to failure’ for the material to allow the redistribution of the applied load over a large area, delaying failure of the film. Fig. 10b shows the H/E ratios of the CrN and Cr<sub>2</sub>N coatings. In general, the MPP CrN coatings exhibited higher H/E ratios (0.080-0.084) as compared to those of the MPP Cr<sub>2</sub>N coating (0.067-0.072) for all coating thicknesses. Therefore, this result indicates that the Cr<sub>2</sub>N coatings exhibit lower toughness and are more brittle than the CrN coatings, which consistent with the fracture toughness results demonstrated by Krishnamurthy et al, using both experimental and modeling approaches [51].

As described in the experimental details section, the nanoindentation hardness of the coatings was also measured on the polished cross-sections of the thick CrN and Cr<sub>2</sub>N coatings to examine the variation of the hardness along the coating thickness within the same coating. A typical example of the measurements on the 20 µm CrN is shown in Fig. 11. It can be seen that the coating only exhibited a slight decrease in the hardness from the bottom to the top. This result further indicates the consistency of the

composition and microstructure of the thick CrN coatings deposited by the MPP technique.

Progressive load scratch testing was used to evaluate the adhesion strength of the thick CrN and Cr<sub>2</sub>N coatings. Fig. 12 shows the graphs of the friction force versus the applied load for progressive load scratch tests on CrN coatings deposited on AISI 440C steel substrate. The sudden rise of the friction force corresponds to the complete failure of the coating, which is referred to the critical load ( $L_c$ ) of the test. This adhesive failure occurred at the interface between the Cr layer and the substrate, as checked by the EDS measurement within the scratch track after the critical failure of the coatings.

As shown in Fig. 12, the  $L_c$  of CrN coatings gradually increased as the coating thickness was increased. The 55 μm CrN coating exhibited a high  $L_c$  of 90 N as compared to a low  $L_c$  of 27 N of the 5 μm CrN coating. As the coating thickness was increased, the load capacity of the coating increased correspondingly since the CrN coating exhibits a much higher hardness and elastic modulus than the steel substrate, thereby leading to an increase in the  $L_c$  of the CrN coatings. Similar observations of the effect of the coating thickness on the scratch test critical load have been widely reported [52].

It is also known that the critical load in a scratch test generally increases with an increase in the substrate hardness [52]. Similar progressive load scratch tests were carried out on the 55 μm CrN and Cr<sub>2</sub>N coatings deposited on the much harder WC-Co substrates in an effort to compare their scratch test critical loads, and the result is shown in Fig. 13. It can be seen that there was no exposure of the substrate and no adhesive failure of the 55 μm CrN coating at the end of the scratch track, which corresponds to a

final normal load of 100 N. However, the 55  $\mu\text{m}$  Cr<sub>2</sub>N coating on cemented carbide substrates showed catastrophic flaking at a 55 N load. Other scratch tests on the CrN and Cr<sub>2</sub>N coatings with different thicknesses also confirmed that the Cr<sub>2</sub>N coating exhibited lower critical loads than the CrN coating at the same coating thickness on the same type of substrates. This result is consistent with an earlier study that showed that the critical load of the hexagonal Cr<sub>2</sub>N is not as high as is cubic CrN due to the brittleness nature in the Cr<sub>2</sub>N coating [45].

Figs. 14a and 14b show the COF and wear rate of the MPP sputtered thick CrN and Cr<sub>2</sub>N coatings sliding against a 5 mm Al<sub>2</sub>O<sub>3</sub> ball, respectively. The typical wear track morphologies of the coatings measured by the profilometer are also illustrated in the figures.

As shown in Fig. 14, the Cr<sub>2</sub>N coatings exhibited higher COF values than those of the CrN coatings with the same coating thickness. This result agrees well with the previous studies on the pulsed dc and dc sputtered CrN and Cr<sub>2</sub>N coatings [44]. It is also noted that the COF values of the CrN and Cr<sub>2</sub>N coatings gradually increased from 0.38 to 0.56 and from 0.55 to 0.71, respectively, as the coating thickness was increased. The increase in the COF for both coatings can be related to an increase in the  $R_a$  (Fig. 9) and a decrease in the hardness of the coatings (Fig. 10) as the coatings grow thicker.

Fig. 14 also demonstrates that the CrN coatings exhibited much lower wear rates than the Cr<sub>2</sub>N coatings for the same thickness. The CrN coatings showed pronounced improvements in the wear resistance as the coating thickness increased above 5  $\mu\text{m}$ . The 2.5  $\mu\text{m}$  thin CrN coating exhibited a wear rate of  $1.1 \times 10^{-6} \text{ mm}^3 \text{N}^{-1} \text{m}^{-1}$ . The wear rate of the CrN coating decreased rapidly as the coating thickness was increased and reached

the lowest value of  $3.5 \times 10^{-7}$  mm<sup>3</sup>N<sup>-1</sup>m<sup>-1</sup> for the 10 µm CrN coating. As the coating thickness was further increased, the wear rates of the coatings slightly increased but were still in the low  $4 \sim 5 \times 10^{-7}$  mm<sup>3</sup>N<sup>-1</sup>m<sup>-1</sup> range. The significant decrease in the wear rate of the thick CrN coatings ( $\geq 10$  µm) as compared to the thin CrN films ( $< 5$  µm) can be attributed to the improved load carrying capacity and the increased scratch critical load (Fig. 12) as the coating thickness was increased. Since the coating is much harder than the stainless steel substrate, the applied normal load during the wear test becomes more substantially supported by the harder coating as the coating thickness is increased.

On the other hand, the Cr<sub>2</sub>N coatings showed higher wear rates in the 3.5 to  $7.5 \times 10^{-6}$  mm<sup>3</sup>N<sup>-1</sup>m<sup>-1</sup> range, which are significantly higher than those of the CrN coatings. By comparing the wear track morphologies of the CrN and Cr<sub>2</sub>N coatings, it can be seen that the wear tracks of the Cr<sub>2</sub>N coatings are much wider and deeper than those of the CrN coatings even after a shorter sliding distance (Fig. 14). The poor wear resistance of the Cr<sub>2</sub>N coating is largely due to its brittleness as indicated by the lower H/E ratio (Fig. 10b) and scratch critical load (Fig. 13) as compared to the CrN coating. It is also widely reported that the Cr<sub>2</sub>N coating exhibited lower thermal stability than the CrN coating [53,54]. Therefore, the Cr<sub>2</sub>N coating exhibits a faster degradation than the CrN coating in terms of the high local temperature generated by the high speed sliding between the coating and sliding counterpart.

#### **4. Conclusions**

The MPP technique has been utilized for reactively sputtering thick Cr<sub>2</sub>N and CrN coatings (up to 55 μm) in a closed field unbalanced magnetron sputtering system with high deposition rates of 15 and 10 μm per hour, respectively. The CrN and Cr<sub>2</sub>N coatings exhibited consistent chemical composition and crystal phase as the thickness of the coating was increased. It was found that both the CrN and Cr<sub>2</sub>N coatings exhibited compressive residual stress. The residual stresses in the CrN and Cr<sub>2</sub>N coatings increased as the coating thickness increased from 2.5 to 30 μm and 20 μm, respectively, but for thicker coatings the stresses decreased. For the investigated coating thickness range, both CrN and Cr<sub>2</sub>N coatings exhibited a nano-columnar microstructure. The CrN coatings showed a denser microstructure than the Cr<sub>2</sub>N coatings, whereas the Cr<sub>2</sub>N coatings exhibited a smaller grain size and surface roughness than those of the CrN coatings for the same coating thickness. The scratch critical load of the CrN coating steadily increased as the coating thickness was increased. The CrN coating exhibited a higher scratch test critical load than the Cr<sub>2</sub>N coating at the same coating thickness. The CrN coatings exhibited lower hardness values but higher H/E ratios than the Cr<sub>2</sub>N coatings for the same coating thickness. Both CrN and Cr<sub>2</sub>N coatings showed a decrease in the hardness and an increase in the sliding COF as the coating thickness increased. However, the wear rate of the CrN coatings decreased significantly as the coating thickness was increase to 10 μm or higher. The 10-55 μm CrN coating exhibited low wear rates in the range of  $3.5\text{--}5 \times 10^{-7}$  mm<sup>3</sup>N<sup>-1</sup>m<sup>-1</sup>. Contrary to the CrN wear test results, the Cr<sub>2</sub>N coating exhibited poor wear resistance in that high wear rates in the range of  $3.5$  to  $7.5 \times 10^{-6}$  mm<sup>3</sup>N<sup>-1</sup>m<sup>-1</sup> were observed for different thicknesses.

## References

---

- [1] N. Kanani, *Electroplating- Basic Principles, Processes and Practice*, Oxford, U.K. (2005).
- [2] L. Pawlowski. *The Science and Engineering of Thermal Spray Coatings*, John Wiley, New York (1995).
- [3] T. Sasaki and K. Kamitani, *J Sol-Gel Sci Technol.* 46 (2008) 180.
- [4] D.A. Karpov, I.F. Kislov, A.I. Ryabchikov, A.A. Ganenko, *Surf. Coat. Technol.* 89 (1997) 58.
- [5] S-S. Zhao, H. Du, J-D. Zheng, Y. Yang, W.Wang, J. Gong, C. Sun, *Surf. Coat. Technol.* 202 (2008) 5170.
- [6] D.W. Wheeler, R.J.K. Wood, *Wear* 225–229 (1999) 523.
- [7] A. Dasgupta, P. A. Premkumar, F. Lawrence, L. Houben, P. Kuppusami, M. Luysberg, K.S. Nagaraja, V.S. Raghunathan, *Surf. Coat. Technol.* 201 (2006) 1401.
- [8] H.M.Soliman and A.F. Waheed, *J. Mater. Sci. Technol.*, 15(5) (1999) 457.
- [9] J. Ullmann, A.J. Kellock, J.E.E. Baglin, *Thin Solid Films* 341 (1999) 238.
- [10] A. Leyland and A. Matthews, *Surf. Coat. Technol.* 70 (1994) 19.
- [11] V. Kouznetsov, K. Macák, J.M. Schneider, U. Helmersson, I. Petrov, *Surf. Coat. Technol.* 122 (1999) 290.
- [12] W. D. Sproul, D. J. Christie, D. C. Carter, *Proceedings of the 47<sup>th</sup> Annual SVC Technical Conference*, Dallas, Texas, April 25-29, 2004, pages 96-100.
- [13] K. Macak, V. Kouznetsov, J.M. Schneider, U. Helmersson, and I. Petrov, *J. Vac. Sci. Technol. A* 18 (2000) 1533.
- [14] D.J. Christie, F. Tomasel, W.D. Sproul, and D.C. Carter, *J. Vac. Sci. Technol. A* 22(4) (2004) 1415.
- [15] Roman Chistyakov, Bassam Abraham, and William D. Sproul, *Proceedings of the 49th Annual SVC Technical Conference*, Washington, DC, April 23-27, 2006, pp. 16-19.

- 
- [16] R. Chistyakov, B. Abraham, W. Sproul, J. Moore, and J. Lin, Proceedings of the 50th Annual SVC Technical Conference, Louisville, KY, April 30 – May 3, 2007, pp. 139-143.
- [17] William D. Sproul, Roman Chistyakov, and Bassam Abraham, Society of Vacuum Coaters News Bulletin, Summer 2006, pp. 35-37.
- [18] J. Lin, J.J. Moore, W.D. Sproul, B. Mishra, Z. Wu, J. Wang, Surf. Coat. Technol. 204 (2010) 2230.
- [19] J. Lin, J.J. Moore, W.D. Sproul, B. Mishra, J.A. Rees, Z. Wu, R. Chistyakov, B. Abraham, Surf. Coat. Technol. 203 (2009) 3676.
- [20] J. Lin, J.J. Moore, W.D. Sproul, B. Mishra, Z. Wu, Thin Solid Films. 518 (2009) 1566.
- [21] V. Kouznetsov, K. Macák, J.M. Schneider, U. Helmersson, I. Petrov, Surf. Coat. Technol. 122 (1999) 290.
- [22] M. Lattemann, A.P. Ehiasarian, J. Bohlmark, P.Å.O. Persson, U. Helmersson, Surf. Coat. Technol. 200 (2006) 6495.
- [23] I. Petrov, P. B. Barna, L. Hultman, and J. E. Greene, J. Vac. Sci. Technol. A 21 (2003) S117.
- [24] D. J. Christie, J. Vac. Sci. Technol. A 23(2) (2005) 330.
- [25] J. Bohlmark, M. Lattemann, J.T. Gudmundsson, A.P. Ehiasarian, Y. Aranda Gonzalvo, N. Brenning, U. Helmersson, Thin Solid Films 515 (2006) 1522.
- [26] J. Lin, J. J. Moore, W. D. Sproul, S. L. Lee, and J. Wang, IEEE Transactions on Plasma Science, (2010), in-press.
- [27] W.D. Sproul, P.J. Rudnik, M.E. Graham, S.L. Rohde, Surf. Coat. Technol. 43/44 (1990) 270.
- [28] I. C. Noyan and J. B. Cohen, Residual Stress Measurement by Diffraction and Interpretation, Springer-Verlag, New York (1987).
- [29] P. Scherrer, Göttinger Nachrichten Gesell. 2 (1918) 98.
- [30] N. Schonberg, Acta Chem. Scand., 8 (1954) 213.

- 
- [31] J. Pelleg, L.Z. Zevin, S. Lungo and N. Croitoru Thin Solid Films 197 (1991) 117.
- [32] C. Nouveau, M.A. Djouadi, O. Banakh, R. Sanjine's, F. Le'vy, Thin Solid Films 398-399 (2001) 490.
- [33] Q.M. Wang and K. H. Kim, J. Vac. Sci. Technol. A 26(5) (2008) 1267.
- [34] Natl. Bur. Stand. (U.S.) Monogr. 25, 21, 63 (1984).
- [35] I. Petrov, L. Hultman, U. Helmersson, J.-E. Sundgren, and J.E. Greene, Thin Solid Films 169, (1989) 299.
- [36] B. Boley, J.H. Weiner, Theory of Thermal Stresses, Kreiger Publishing, Florida, 1985.
- [37] ASM Specialty Handbook: Stainless Steels, ASM International, Materials Park, OH, USA (1994).
- [38] F-H. Lu, H-Y. Chen, and C-H. Hung, J. Vac. Sci. Technol. A 21.3., (2003) 671.
- [39] K. Taneichi, T. Narushima, Y. Iguchi, C. Ouchi, Materials Transactions, 47(10) (2006) 2540.
- [40] Y. Kenji, S. Toshiki, I. Eiji, Journal of the Surface Finishing Society of Japan, 50(1) (1999): 52-57.
- [41] W.Herr, B. Matthes and E. Broszeit, Surf. Coat. Technol. 60 (1993) 428.
- [42] S.J. Bull, A.M. Jones, A.R. McCabe, Surf. Coat. Technol. 54 (1992) 173.
- [43] C. V. Thompson, Annu. Rev. Mater. Sci., 20 (1990) 245.
- [44] J. Lin, Z.L. Wu, X.H. Zhang, B. Mishra, J. J Moore, W. D. Sproul, Thin Solid Films 517 (2009) 1887.
- [45] T. Hurkmans, D.B. Lewis, J.S. Brooks, W.D. Munz, Surf. Coat. Technol. 86-87 (1996) 192.
- [46] F. Papa, R. Tietema, T. Krug, and A. Campiche, 52nd Annual Technical Conference Proceedings, Santa Clara, CA, May 9–14, 2009, pages 214-218.
- [47] J. Langner, M.J. Sadowski, P. Strzyzewski, R Mirowski, et al., XXIIInd Int. Symp. on Discharges and Electrical Insulation in Vacuum, Matsue, (2006) 535.
- [48] E. O. Hall, Proc. Phys. Soc. London, Sect. B 64, (1951) 747.

- 
- [49] Leyland A, Matthews A. Wear 246 (2000) 1.
- [50] Musil J, Jirout M. Surf Coat Technol 201 (2007) 5148.
- [51] S. Krishnamurthy, I. E. Reimanis, J. Berger, and E. Drexler, J. Am. Ceram. Soc., 87 (7) (2004) 1306.
- [52] A.J. Perry. Thin Solid Films 107 (1983) 167.
- [53] M. -A. Djouadi, C. Nouveau, O. Banakh, R. Sanjinés, F. Lévy and G. Nouet, Surf. Coat. Technol. 151-152 (2002) 510.
- [54] J. Lin, B. Mishra, J.J. Moore, and W.D. Sproul, Surf. Coat. Technol. 202 (2008) 3272.

Table 1: The deposition conditions for the Cr interlayer, CrN and Cr<sub>2</sub>N coatings.

	P <sub>a</sub> [k W]	P <sub>p</sub> [k W]	I <sub>a</sub> [A ]	I <sub>p</sub> [A]	V <sub>a</sub> [V]	V <sub>p</sub> [V]	Repetiti on rate [Hz]	Peak I <sub>sub</sub> [mA/c m <sup>2</sup> ]	Mean I <sub>sub</sub> [mA/c m <sup>2</sup> ]	Pressu re [Pa]	Ar: N <sub>2</sub>	Bia s [V]	Deposi tion rate [μm/ho ur]
Cr lay er	1.5	108	9 1	20 0	46 6	62 2	30	350	66.2	0.67	1:0	-5 0	8
CrN	3.0	95	8 3	19 0	46 3	57 5	73	302	58.8	0.67	1:1	-5 0	10
Cr <sub>2</sub> N	3.0	100	8 1	18 4	47 0	61 5	70	295	53.8	0.67	3:1	-5 0	15

- P<sub>a</sub> and P<sub>p</sub> are the average and peak target powers;
- I<sub>a</sub> and I<sub>p</sub> are the average and peak target currents in one pulse length;
- V<sub>a</sub> and V<sub>p</sub> are the average and peak target voltages;
- I<sub>sub</sub> is the substrate ion current density

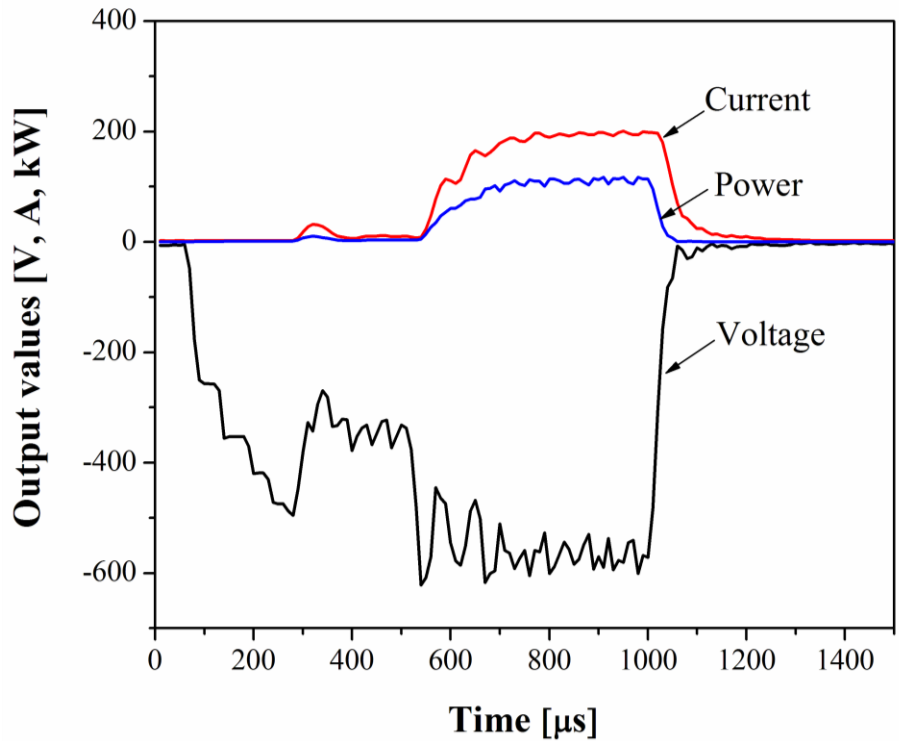


**Figure 1:** The target voltage, current and power waveforms during one modulated pulse used for the depositions.

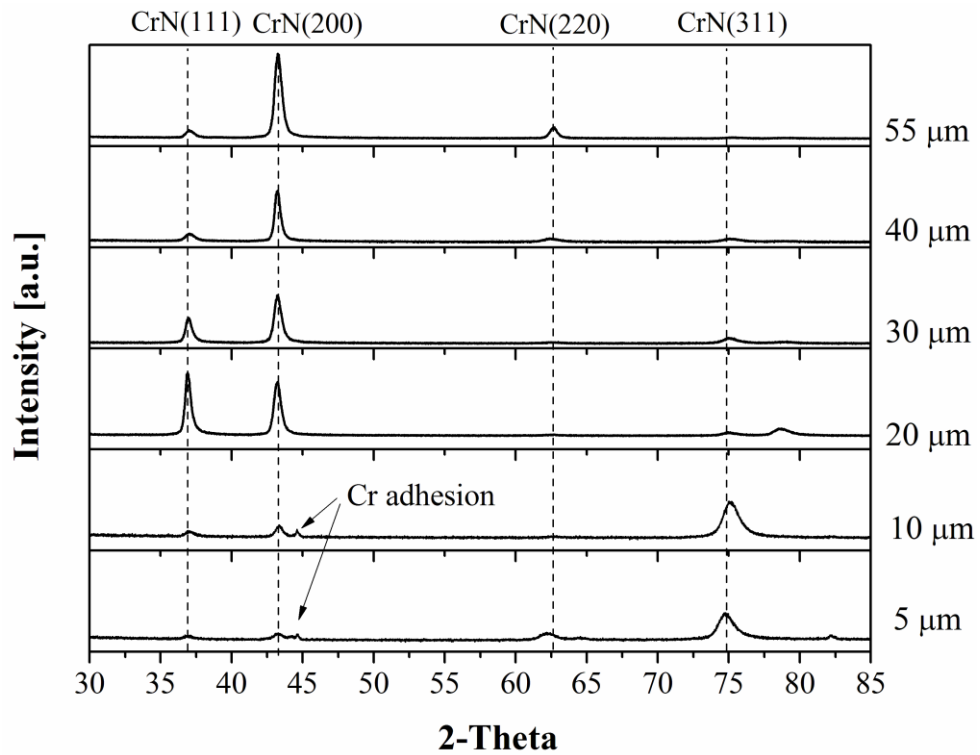


**Figure 2a:** XRD patterns of the MPP sputtered CrN coatings with different coating thicknesses.

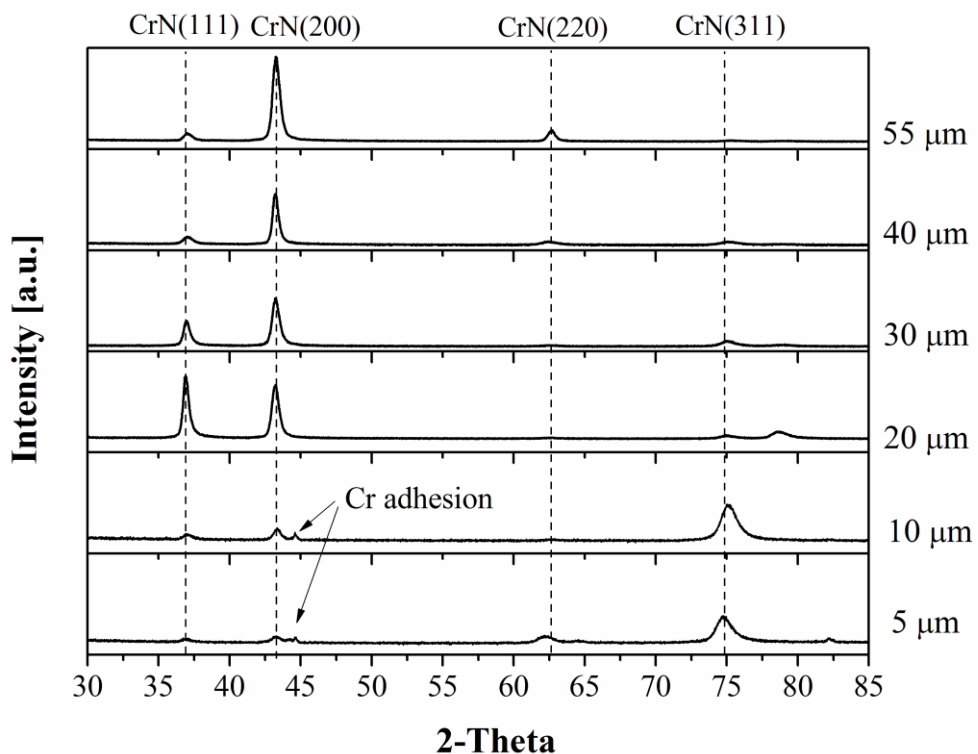


**Fig. 2b: XRD patterns of the MPP sputtered Cr<sub>2</sub>N coatings with different coating thicknesses.**

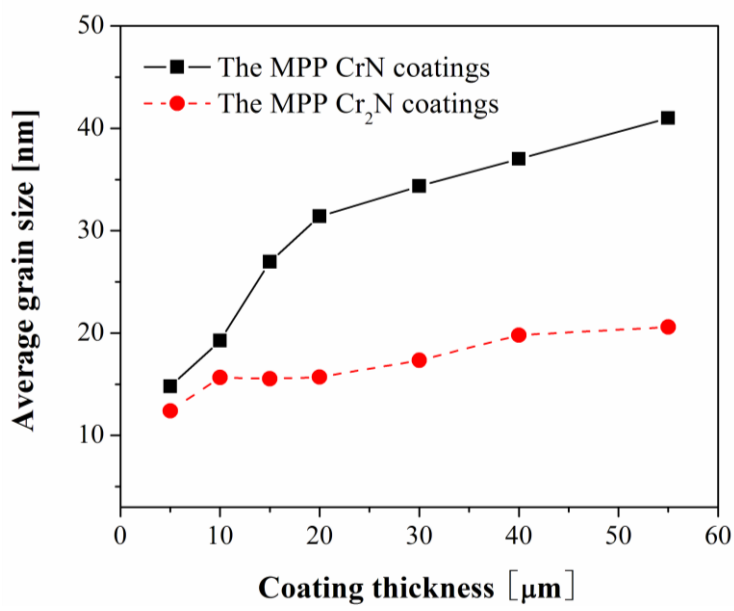


**Figure 3: Effect of the coating thickness on the average grain size of the MPP CrN and Cr<sub>2</sub>N coatings.**

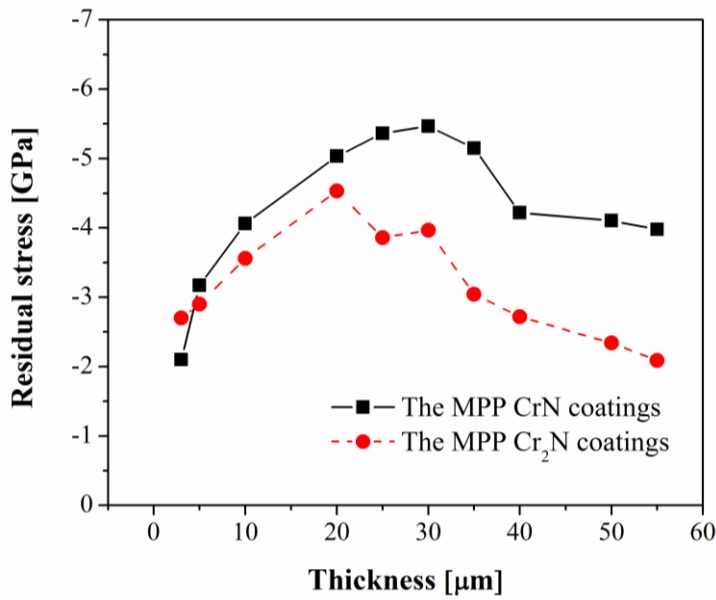


**Figure 4: Dependence of the residual stresses of the MPP CrN and Cr<sub>2</sub>N coatings on the coating thickness.**

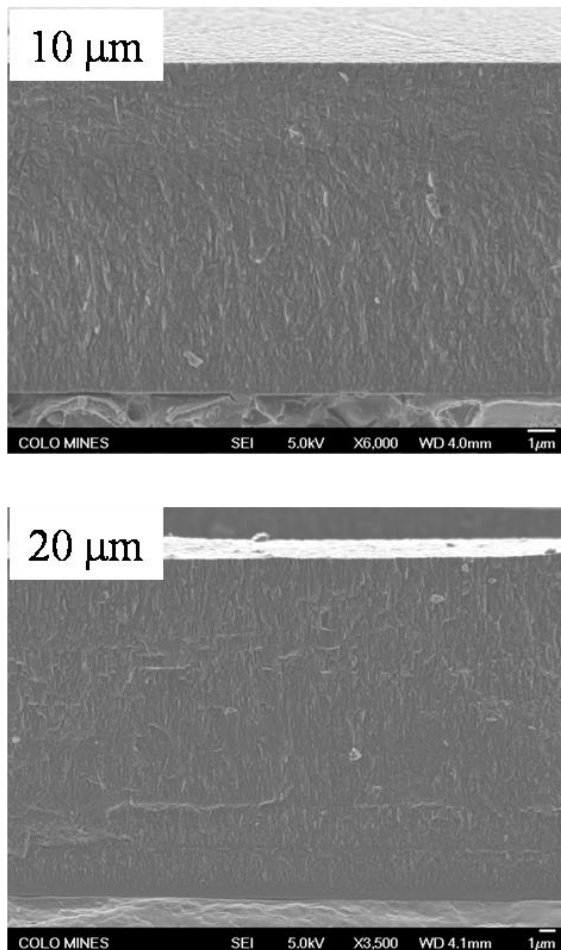


**Figure 5:** Cross-sectional SEM micrographs of the MPP sputtered CrN coatings with different thicknesses a) 10  $\mu\text{m}$ , b) 20  $\mu\text{m}$ , c) 30  $\mu\text{m}$  and d) 55  $\mu\text{m}$ .

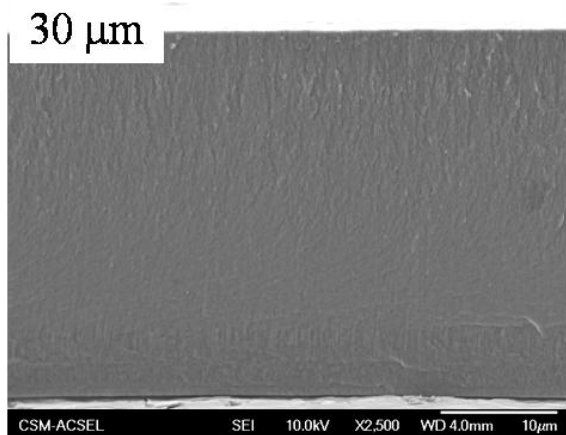
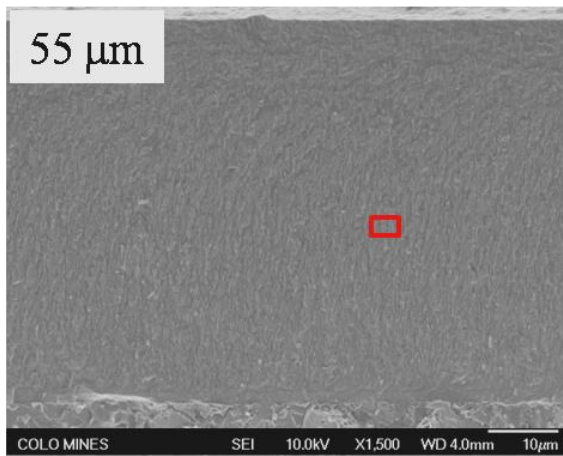
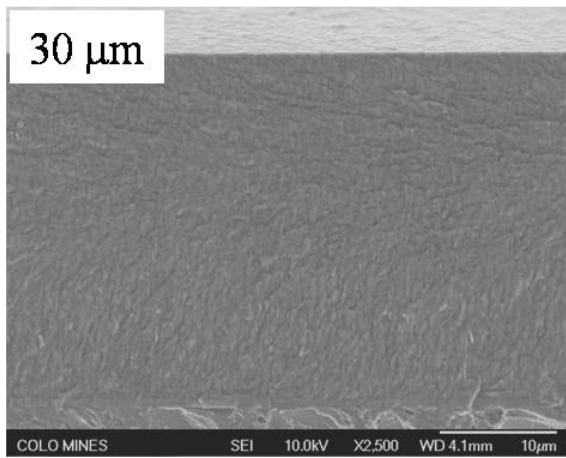


**Figure 5 (continued): Cross-sectional SEM micrographs of the MPP sputtered CrN coatings with different thicknesses a) 10  $\mu\text{m}$ , b) 20  $\mu\text{m}$ , c) 30  $\mu\text{m}$  and d) 55  $\mu\text{m}$ .**

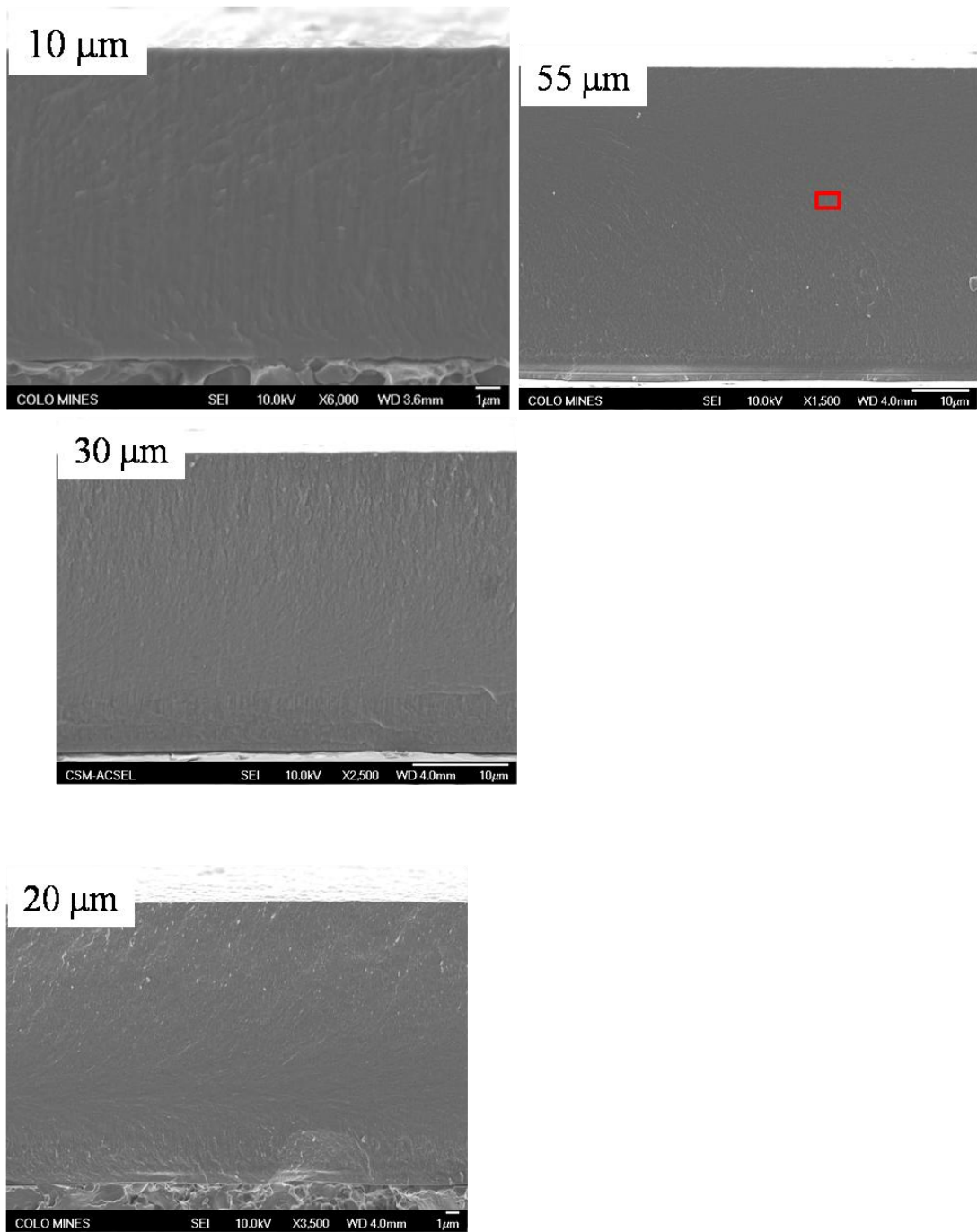
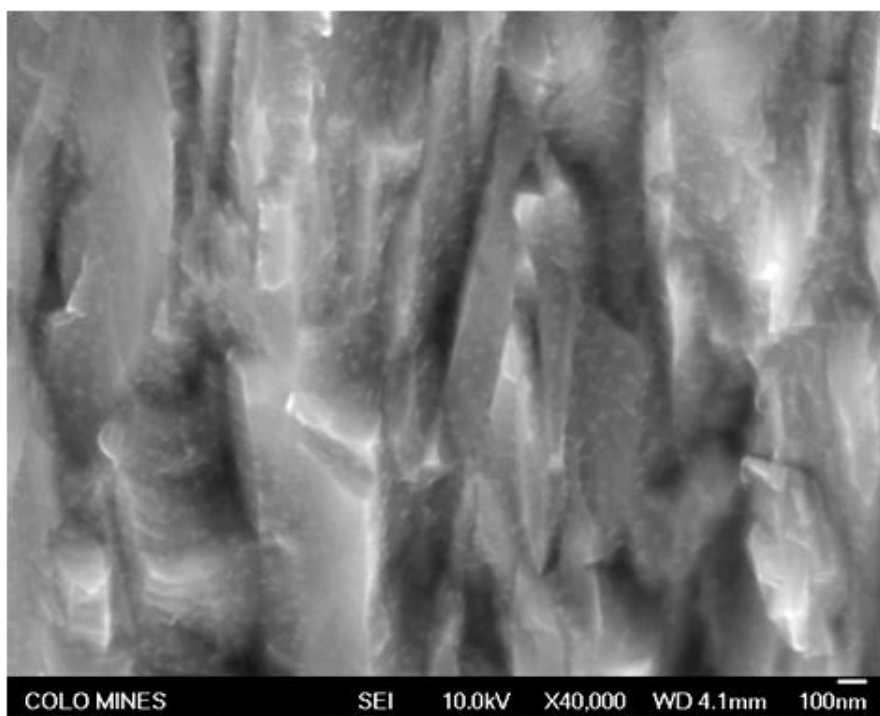
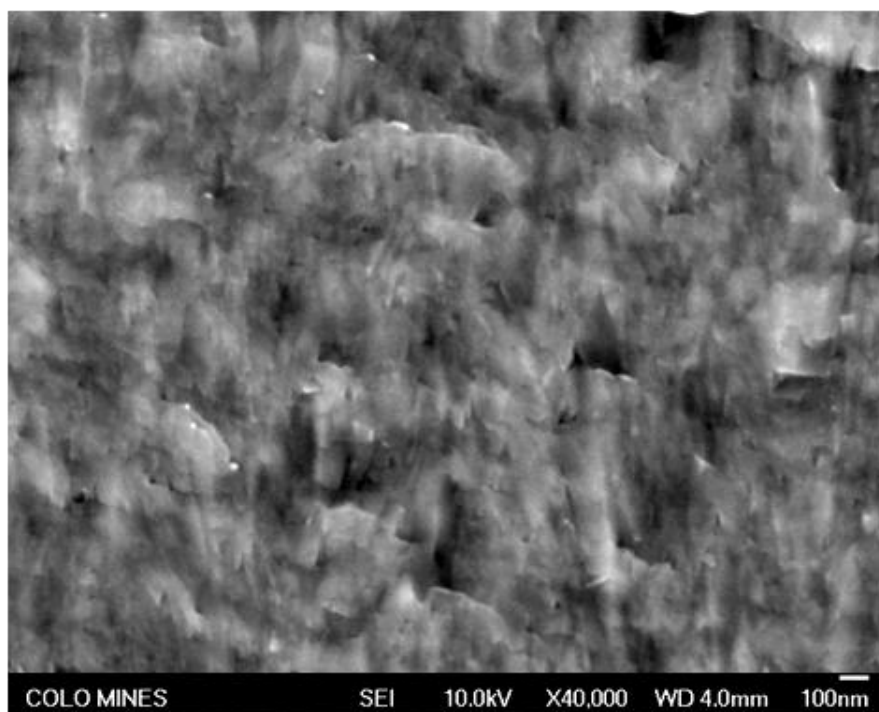


**Figure 6: Cross-sectional SEM micrographs of the MPP sputtered Cr<sub>2</sub>N coatings with different thicknesses a) 10 μm, b) 20 μm, c) 30 μm and d) 55 μm.**



COLO MINES

SEI 10.0kV X40,000 WD 4.1mm 100nm



COLO MINES

SEI 10.0kV X40,000 WD 4.0mm 100nm

**Figure 7: Cross-sectional SEM micrographs of the microstructure of the 55  $\mu\text{m}$  a) CrN and b) Cr<sub>2</sub>N coatings as observed in the box marked in Figure 5d and Figure 6d.**

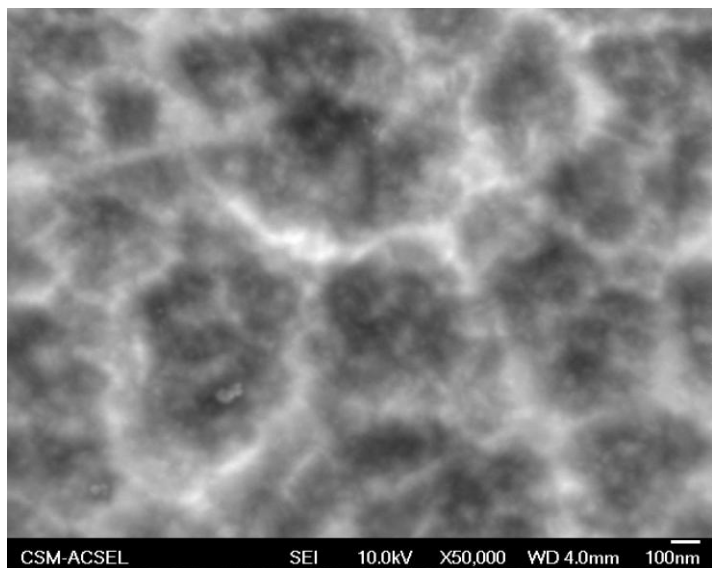
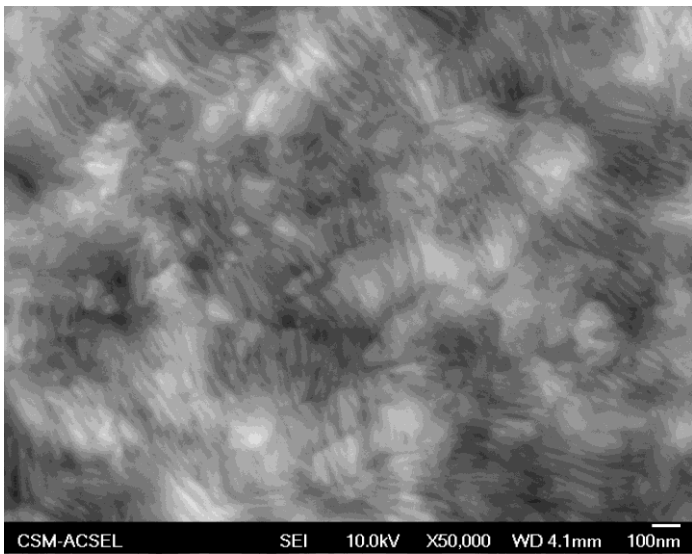


**Figure 8: Top view SEM micrographs of the 55  $\mu\text{m}$  a) CrN and b)  $\text{Cr}_2\text{N}$  coatings.**

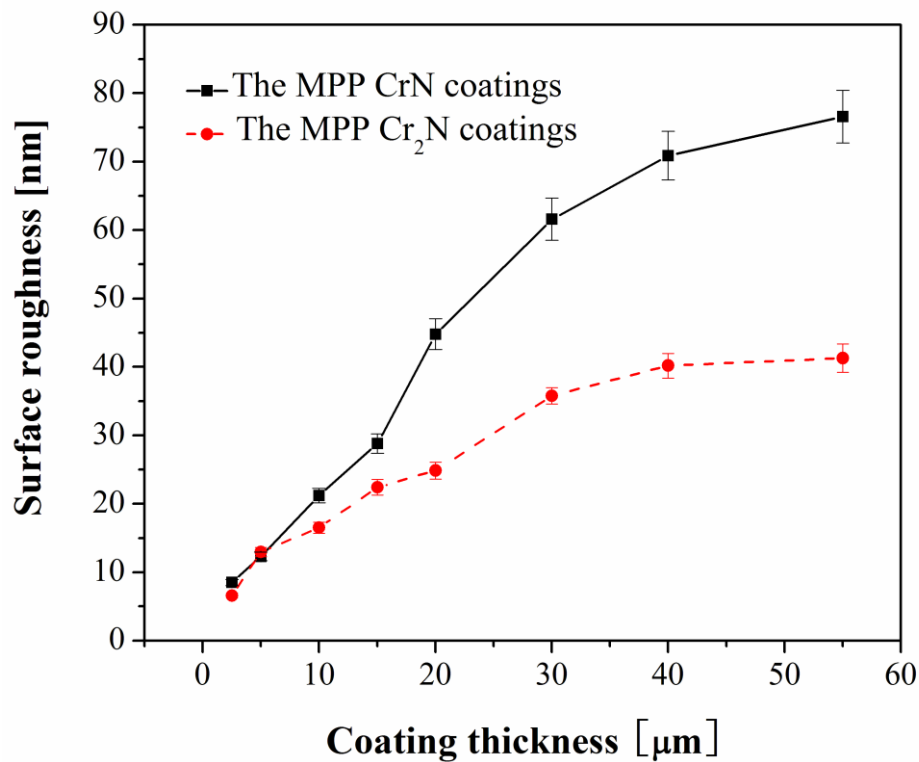


**Figure 9: Effect of the coating thickness on the average surface roughness ( $R_a$ ) of the MPP sputtered CrN and Cr<sub>2</sub>N coatings.**

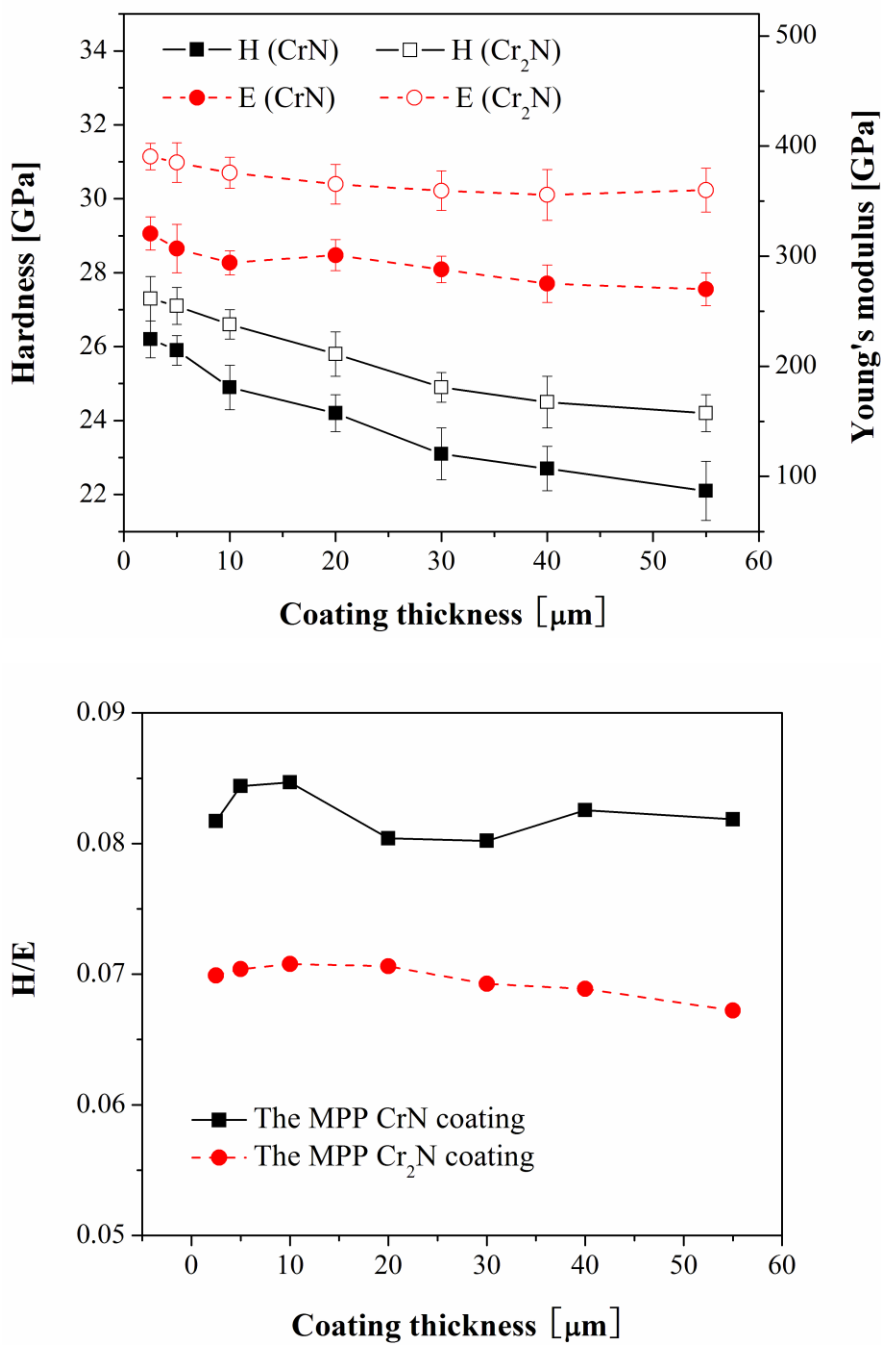


**Figure 10: a) Hardness and Young's modulus and b) the H/E ratios of the MPP sputtered CrN and Cr<sub>2</sub>N coatings with different coating thicknesses.**

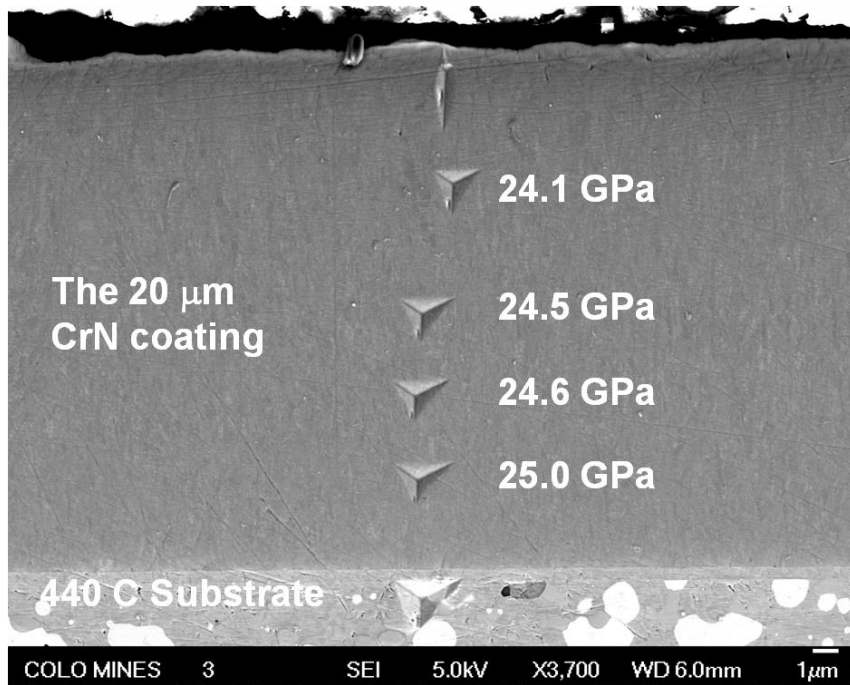


**Figure 11:** Cross-sectional SEM micrographs showing the nanoindentation test performed on the polished cross-section of the 20  $\mu\text{m}$  CrN coating along the coating thickness.

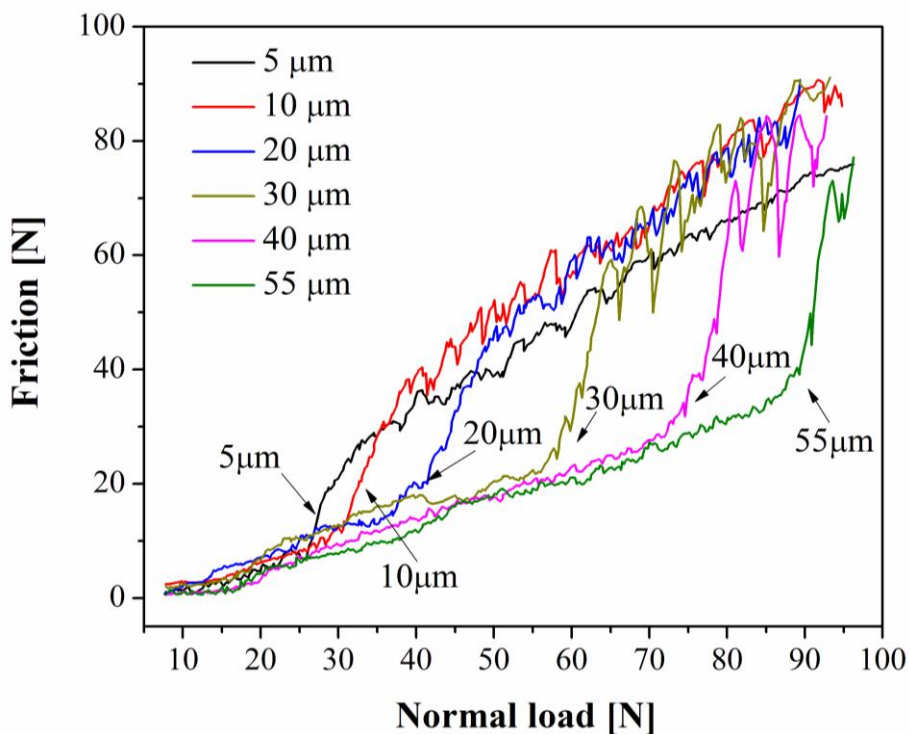


**Figure 12:** Friction force versus the applied load during the progressive load scratch tests performed on the CrN coatings deposited on AISI 440C steel substrate with different coating thicknesses.

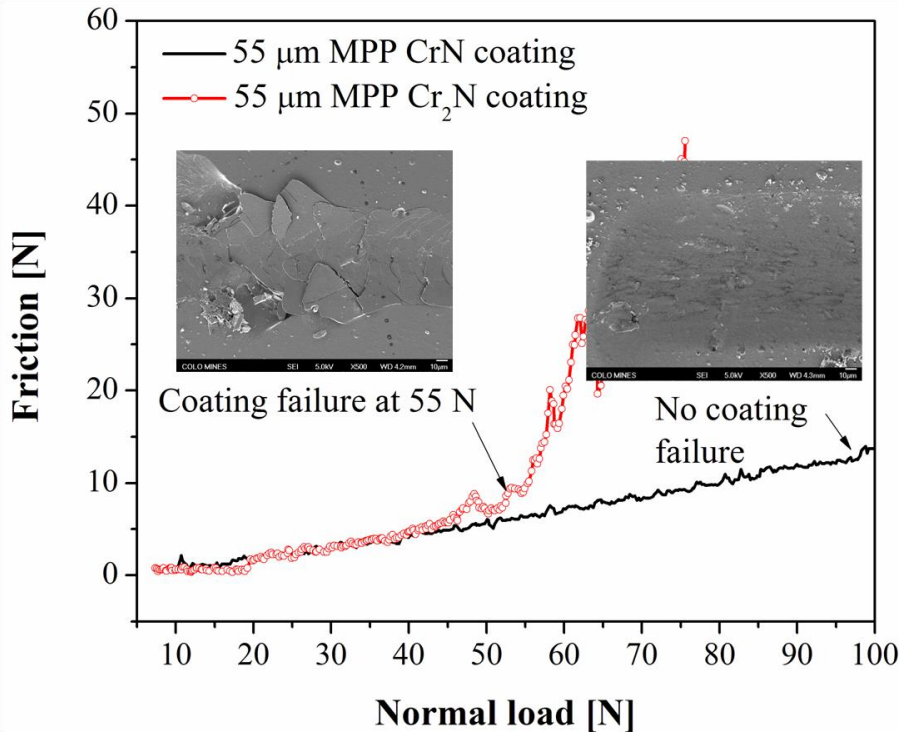


**Figure 13:** Friction force versus applied load during the progressive load scratch tests performed on the 55  $\mu\text{m}$  CrN and Cr<sub>2</sub>N coatings deposited on WC-Co substrate. (The insert SEM micrographs show the beginning of the adhesive failure of the Cr<sub>2</sub>N coating and the end of the scratch track of the CrN coating).

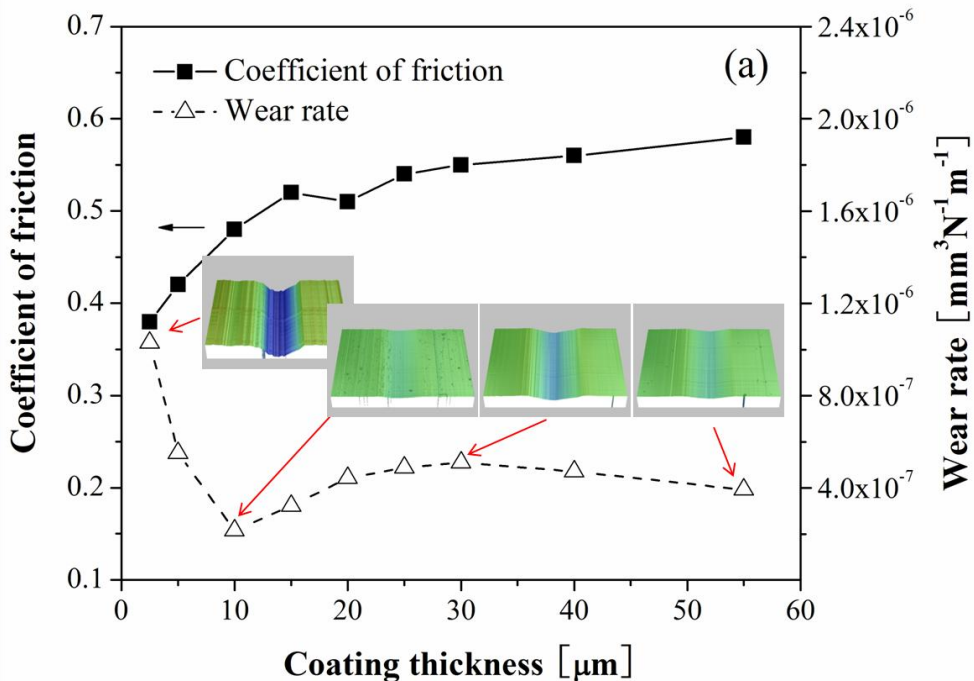


**Figure 14:** Coefficient of friction and wear rate of the MPP sputtered a) CrN and b) Cr<sub>2</sub>N coatings with different coating thicknesses.